A new delay time distribution for merging neutron stars tested against Galactic and cosmic data

Paolo Simonetti [1,2]★ Francesca Matteucci,[1,2,3] Laura Greggio[4] and Gabriele Cescutti [2]

[1]*Dipartimento di Fisica, Sezione di Astronomia, Università degli Studi di Trieste, Via G. B. Tiepolo 11, I-34143 Trieste, Italy*
[2]*INAF, Osservatorio Astronomico di Trieste, Via G.B. Tiepolo 11, I-34143 Trieste, Italy*
[3]*INFN, Trieste, Via A. Valerio 2, I-34127 Trieste, Italy*
[4]*INAF, Osservatorio Astronomico di Padova, Vincolo dell'Osservatorio 5, I-35122 Padova, Italy*

ABSTRACT

The merging of two neutron stars (MNS) is thought to be the source of short gamma-ray bursts (SGRB) and gravitational wave transients, as well as the main production site of r-process elements like Eu. We have derived a new delay time distribution (DTD) for MNS from theoretical considerations and we have tested it against (i) the SGRB redshift distribution and (ii) the Galactic evolution of Eu and Fe, in particular the [Eu/Fe] versus [Fe/H] relation. For comparison, we also tested other DTDs, as proposed in the literature. To address the first item, we have convolved the DTD with the cosmic star formation rate, while for the second we have employed a detailed chemical evolution model of the Milky Way. We have also varied the DTD of Type Ia SNe (the main Fe producers), the contribution to Eu production from core-collapse SNe, as well as explored the effect of a dependence on the metallicity of the occurrence probability of MNS. Our main results can be summarized as follows: (i) The SGRB redshift distribution can be fitted using DTDs for MNS that produce average time-scales of 300–500 Myr; (ii) If the MNS are the sole producers of the Galactic Eu and the occurrence probability of MNS is constant the Eu production time-scale must be on the order of $\lesssim$30 Myr; (iii) Allowing for the Eu production in core-collapse SNe or adopting a metallicity-dependent occurrence probability, allow us to reproduce both observational constraints, but many uncertainties are still present in both assumptions.

Key words: nuclear reactions, nucleosynthesis, abundances – gamma-ray burst: general – stars: neutron – Galaxy: evolution.

1 INTRODUCTION

The merging of two neutron stars via the emission of gravitational waves has been invoked to explain a variety of phenomena like the production of heavy r-process elements (Korobkin et al. 2012; Hotokezaka et al. 2013) and the short gamma-ray bursts (SGRBs; Eichler et al. 1989; Narayan, Paczynski & Piran 1992). The observation of binary systems composed by compact and massive star remnants (Hulse & Taylor 1975; Tauris et al. 2017) with measurable changes in their orbital periods, and the recent detection of the gravitational wave (GW) transient GW170817 (Abbott et al. 2017a) strongly support the occurrence of this process.

Elements heavier than Fe cannot be produced by exoenergetic fusion reactions in stars and instead they must be the result of

neutron capture on Fe-peak nuclei. This capture can be 'rapid' or 'slow' with respect to the β decay time-scale and produces two distinct abundance patterns (Burbidge et al. 1957; Seeger, Fowler & Clayton 1965). Correspondingly, these elements are called r- and s-process elements, depending on which of these processes has contributed the most to their production at solar metallicity. Moreover, r-process elements can be subdivided in a light (with atomic weight $A < 90$) and a heavy ($A > 90$) subclass. A widespread used tracker for heavy r-process elements is Europium (Eu; e.g. Matteucci et al. 2014). The production of heavy r-process elements requires very neutron-rich environments, such as core-collapse SNe (CC–SNe) and MNS. The dominant production site, though, remains uncertain (Côté et al. 2018a).

Early studies, based on the observation of r-process elements in very metal-poor ([Fe/H] < -3.0 dex) stars, led to the conclusion that r-process production should occur in massive, short-lived stars ($m > 10\,\mathrm{M_\odot}$, Truran 1981).

★ E-mail: paolo.simonetti@inaf.it

Hydrodynamical simulations (e.g. Woosley et al. 1994; Wheeler, Cowan & Hillebrandt 1998) supported such a result, showing that the neutrino-driven wind from newly born neutron stars (NS) in stars with masses higher than 20 $M_\odot$ is a promising (although imperfect) site for r-process nucleosynthesis. However, subsequent studies (Arcones, Janka & Scheck 2007; Arcones & Janka 2011; Martínez-Pinedo et al. 2012) have cast doubts on the capability of this mechanism to produce a robust r-process abundance pattern. In particular, it was found that neutrino-driven winds were not enough neutron rich to produce elements with $A > 120$. Moreover, the final abundance pattern is very sensitive to details of the physical conditions at explosion. Other simulations have identified two possible regions inside a collapsar in which heavy r-process production can occur. The first one is constituted by the polar jets accelerated by extreme magnetic fields in a rare sub-class of CC–SNe called magnetorotational (MR) SNe (Cameron 2003; Winteler et al. 2012). The second one is constituted by the outflows from the accretion disc around the newly formed central compact object which have been claimed to put broader constraints on the initial physical conditions than the MR–SNe case (Siegel, Barnes & Metzger 2018). However, it is not clear if their rate is sufficient to reproduce the solar abundance of r-process elements (Woosley & Heger 2006). If this is the case, collapsars would be an adequate primary r-process site (Cescutti & Chiappini 2014).

In parallel, other authors have explored the role of compact object mergers (CBM; like NS–NS and NS–BH systems) in the production of r-process elements. Nucleosynthesis calculations (Korobkin et al. 2012; Eichler et al. 2015; Rosswog 2015) predict the ejection of up to 10^{-2} $M_\odot$ of r-process matter with a robust abundance pattern in a single coalescence event, due to the large number of neutrons per target Fe nuclei. There are some uncertainties on the role of neutron poorer viscous and neutrino-driven ejecta from CBM accretion discs (see e.g. Martin et al. 2015; Wu et al. 2016), but this source appears to be more reliable with respect to the CC–SNe.

The viability of double neutron star mergers as r-process production site has been tested in Galactic chemical evolution simulations, which trace the abundances of different elements in the gas of the Milky Way. In this regard, a very important parameter to evaluate is the time-scale of production of a given element, which can be estimated as the average coalescence time-scale of a single burst stellar population. For MNS systems, the delay time (or time between the birth of the binary system and its final merging) is determined by both the stellar nuclear lifetime and the gravitational delay time, and it can vary in a wide range. The typical time-scale for enrichment from MNS depends on the distribution of the delay times (DTD).

A popular choice in literature consist in selecting a DTD in the form of a power law, i.e. $\propto t^{-\gamma}$ with $0.5 \leq \gamma \leq 2.0$ (Côté et al. 2017b; Hotokezaka, Beniamini & Piran 2018), where t is the total (i.e. nuclear + gravitational) coalescence delay time; in other studies, the total coalescence delay time is obtained by adding a constant gravitational delay on top of stellar evolutionary lifetimes (Matteucci et al. 2014; Vangioni et al. 2015). Some authors, like Matteucci et al. (2014), have tested both MNS only, and a combination of MNS and CC–SNe as Eu producers. In all studies it is found that, in order to reproduce the decreasing trend in the [Eu/Fe] versus [Fe/H] relation in the thin disc stars, the Europium pollution time-scale should not exceed 100 Myr or be even shorter (10–30 Myr). These time-scales can be attained either using very steep power laws ($\propto t^{-2}$) or assuming a constant gravitational delay of 1 Myr on top of the nuclear evolution time-scale of the progenitors. These DTDs are in disagreement with the results of

population synthesis models (Belczynski et al. 2017; Côté et al. 2018a; Giacobbo & Mapelli 2018b) that predict a γ in the range $[-1.0; -1.5]$.

Gamma-ray bursts (GRBs) are luminous transients of high-energy photons (in the range of 10–100 keV) incoming isotropically to the Earth at a rate of 1 per day (Klebesadel, Strong & Olson 1973). They can be divided in short (<2 s, SGRBs) and long (>2 s, LGRBs; Norris et al. 1984); SGRBs are characterized by high-peak energy, while LGRBs exhibit a softer emission. It is generally accepted that short and long GRBs are produced by different mechanisms; in particular the latter have been explained as due to the acceleration of matter along the poles of a newly born black hole during massive CC–SNe explosions (MacFadyen & Woosley 1999). The SGRBs are instead thought to be produced from the magnetic recombination or neutrino–antineutrino annihilation during the merging of compact binary objects (Narayan et al. 1992).

Despite the small statistics, various groups (Ghirlanda et al. 2016; Zhang & Wang 2018) have reconstructed the redshift distribution of SGRBs, while others (D'Avanzo 2015; Fong et al. 2017) have tried to reproduce it by convolving different DTDs with the cosmic star formation history. It has been found that the SGRB redshift distribution is better reproduced when a DTD $\propto t^{-1}$ or $\propto t^{-1.5}$ is used. Moreover, between 1/4 and 1/3 of the total SGRBs comes from early-type galaxies (Berger 2014; Fong et al. 2017), which host old stellar populations. This evidence contrasts with the notion of short time-scales to describe MNS in favour of longer ones.

A great deal of information comes from the detection of GW170817. Not only it has been the first direct evidence of an MNS (Abbott et al. 2017a), but it was also associated with an SGRB (Abbott et al. 2017b) and an optical transient known as 'kilonova' (Smartt et al. 2017). The study of its multiband light curves and of the spectra has provided constraints on the composition of the ejecta, though a consensus has not yet been reached. Smartt et al. (2017) concluded that these ejecta should have been rich in light r-process and very deficient in heavy r-process, while others (Evans et al. 2017; Pian et al. 2017; Tanvir et al. 2017; Troja et al. 2017) support the hypothesis of a robust production of extremely opaque r-process elements. Finally, based on this event, Abbott et al. (2017a) estimated the cosmic local rate of MNS events to be 1540^{+3200}_{-1220} yr^{-1} Gpc^{-3}.

In this paper we want to test under which conditions it is possible to accommodate the various observational constraints under the hypothesis that MNS are responsible for all SGRBs, and that they are important contributors to the Europium chemical enrichment of the Milky Way. To do this we: (i) derive a new formulation for the DTD from theoretical considerations, adapting the Greggio (2005) procedure, which was developed for Type Ia Supernovae, to the progenitors of MNS; (ii) use the cosmic star formation history (CSFR) and the redshift distribution of SGRBs to evaluate the fraction of massive stars, which give rise to a MNS event; (iii) test the results versus the Milky Way abundance pattern of Eu and Fe using a full Galactic chemical evolution model of the Milky Way, which successfully reproduces a majority of observational constraints (e.g. Matteucci et al. 2009). We also explore the effect of adopting the DTD formulations which are proposed in the literature.

2 OUR NEW DTD

The DTD function $f_{MNS}(\tau)$ for MNS represents the distribution of the coalescence times from an instantaneous burst of star formation of unitary mass and it is fundamental to compute the MNS rate. The

MNS rate can be written as

$$R_{MNS}(t) = k_\alpha \int_{\tau_i}^{\min(t,\tau_x)} \alpha_{MNS}(\tau)\,\psi(t-\tau)\,f_{MNS}(\tau)\,d\tau, \qquad (1)$$

where ψ is the SFR, k_α is the number of stars with mass in a suitable range per unit mass of star-forming gas in a stellar generation, and α_{MNS} is the fraction of them which gives rise to MNS events. In principle, both k_α and α_{MNS} can vary as a function of time, but for the sake of simplicity we will assume them constant. In Section 5.4 we will explore the effect of varying α_{MNS}. The time τ is the delay time defined in the range (τ_i, τ_x), where τ_i is the minimum delay time of occurrence for merging neutron star (here fixed to 10 Myr) and τ_x is the maximum delay time which can be larger than a Hubble time, depending on the progenitor model. Since $f_{MNS}(\tau)$ is a distribution function, it must be normalized to 1 in the allowed range for τ:

$$\int_{\tau_i}^{\tau_x} f_{MNS}(\tau)\,d\tau = 1. \qquad (2)$$

The parameter k_α depends on the IMF and it is

$$k_\alpha = \int_{m_L}^{m_U} \phi(m)\,dm, \qquad (3)$$

where m_L and m_U are, respectively, the progenitor minimum and maximum mass to produce an NS. In this paper we adopt $m_L = 9\,M_\odot$ and $m_U = 50\,M_\odot$.

We now derive the form of $f_{MNS}(\tau)$. For MNS the time delay is the sum of the evolutionary lifetime of the secondary component of the binary system plus the gravitational time delay. From Landau and Lifshitz (1966):

$$\tau_{gw} = \frac{0.15A^4}{m_1 m_2(m_1 + m_2)}\,Gyr, \qquad (4)$$

where m_1 and m_2 are the masses of the primary (more massive) and of the secondary star of the binary system, respectively, while A is the initial separation of the neutron star binary system. We have neglected the eccentricity parameter for the sake of simplicity. In fact, for high eccentricity the coalescence time can be much shorter, at fixed values of masses and separations, but here we consider only the case of circular orbits.

We can now show that this equation can be rewritten as a function of the total mass, instead of the masses of the two components, with a small error. The mass-dependent term, namely the denominator of equation (4), can be written as

$$\mu(M_{DN}, m_2) = M_{DN}^2 \cdot m_2 - m_2^2 \cdot M_{DN}, \qquad (5)$$

with $M_{DN} = m_1 + m_2$, i.e. the total mass of the system. This function can be studied in its two variables. For a fixed M_{DN} this formula produces a parabola with the maximum at $m_2 = 0.5\,M_{DN}$.

The lightest known neutron star whose mass has been precisely measured is the companion of the binary pulsar PSR J0453+1559, with an estimated mass of $1.17 \pm 0.004\,M_\odot$ (Martinez et al. 2015). On the other hand, the heaviest measured neutron star is the PSR J0348+0432, with a mass of $2.01 \pm 0.04\,M_\odot$ (Antoniadis et al. 2013). In a yet not fully confirmed study, Linares, Shahbaz & Casares (2018) estimate the mass of PSR J2215+5135 to be $2.27 \pm 0.15\,M_\odot$, and this fact would rule out some of the proposed equations of state for NS interior (Özel & Freire 2016).

We have decided to adopt a slightly different range with a lower limit to the mass of the neutron star of $1\,M_\odot$ and an upper limit of $2\,M_\odot$. Therefore the allowed range for M_{DN} goes from 2.0 to 4.0 $M_\odot$. The requirements on the mass of the primary NS further constrains the range of possible values for m_2 so that not all combinations of
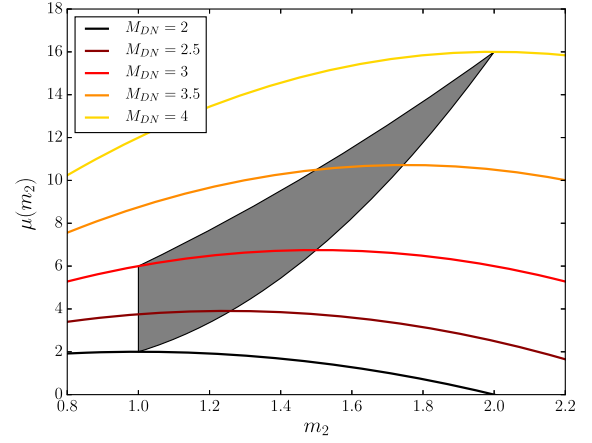
Figure 1. The function $\mu(M_{DN}, m_2)$ is plotted with respect to m_2 for five different fixed values of M_{DN} (2.0 $M_\odot$ in black, 2.5 $M_\odot$ in dark red, 3.0 $M_\odot$ in red, 3.5 $M_\odot$ in orange, and 4.0 $M_\odot$ in yellow solid lines). The grey shaded area represents the space of valid values for m_2 (i.e. represents a system with a secondary lighter than the primary and in the correct mass range, for a fixed total mass of the system).

M_{DN} and m_2 are acceptable. In Fig. 1 we show the function $\mu(M_{DN}, m_2)$ plotted versus m_2 for five different values of M_{DN}. The shaded area shows the portion of the plane in which $m_1 > m_2$. The sections of the parabolae within the shaded area are very flat: for each M_{DN} the function μ varies very little (no more than 10 per cent) inside the allowed region of the parameter space (m_1, m_2).

We can conclude that it is possible to rewrite μ as a function of M_{DN} with a negligible error: every binary system with the same total mass and the same initial separation has approximately the same delay. Substituting the value of the maximum for each M_{DN}, $\mu(M_{DN}, m_2)$ becomes

$$\mu(M_{DN}) = 0.25 M_{DN}^3, \qquad (6)$$

and so it follows that

$$\tau_{gw} = \frac{0.6A^4}{M_{DN}^3}\,Gyr. \qquad (7)$$

Having simplified the Landau formula we derive distribution of the delay times due to the emission of gravitational waves as follows.

The contribution to the number of systems with delay τ_{gw} from systems with separation A and total mass M_{DN} can be written as

$$df(\tau_{gw}) = df(A, M_{DN}) = g(A)\,h(M_{DN})\,dA\,dM_{DN}, \qquad (8)$$

where $g(A)$ is a function describing the initial separations, while $h(M_{DN})$ is the distribution of the total masses of the systems that will merge. In equation (8) these two functions are assumed to be independent. We further assume that $g(A)$ can be described as a power law and, for simplicity, that the distribution of binary masses is flat. Therefore the two functions can be written as

$$\begin{cases} g(A) \propto A^\beta \\ h(M_{DN}) \propto const. \end{cases} \qquad (9)$$

As can be seen, β parametrizes the shape of the distribution in initial separations. Integrating equation (8) over the relevant range of separations we derive the number of MNS systems, which merge with a gravitational time delay τ_{gw}:

$$f(\tau_{gw})d\tau_{gw} = d\tau_{gw}\int_{A_l}^{A_s} g(A)\,h(M_{DN})\left|\frac{\partial M_{DN}}{\partial \tau_{gw}}\right| dA, \qquad (10)$$

with A_l and A_s are the minimum and maximum separations that contribute to $n(\tau_{\rm gw})$ for systems with total mass $M_{\rm DN}$. They can be calculated as

$$A_x = \left(\frac{M_{{\rm DN},x}^3 \tau_{\rm gw}}{0.6} \right)^{1/4}, \tag{11}$$

where the subscript x stands for s and l. The result of such calculation is

$$f(\tau_{\rm gw}) \propto \frac{1}{\tau_{\rm gw}^{4/3}} \frac{1}{\beta + 7/3} \left[A^{\beta + 7/3} \right]_{A_l}^{A_s}. \tag{12}$$

Substituting equation (11) in equation (12) we derive the distribution of the gravitational wave delay times as

$$f(\tau_{\rm gw}) \propto \tau_{\rm gw}^{(1/4)\beta - 3/4} \left(M_{{\rm DN},s}^{(3/4)(\beta + 7/3)} - M_{{\rm DN},l}^{(3/4)(\beta + 7/3)} \right). \tag{13}$$

The number of systems with a total delay between τ and $\tau +$ dτ will be close to the number of systems with a gravitational delay between $\tau_{\rm gw}$ and $\tau_{\rm gw} +$ d$\tau_{\rm gw}$, because of the short and similar nuclear lifetime (τ_n) of stars with high masses, that ranges between $\sim$30 Myr for 9 $M_\odot$ stars and $\sim$4 Myr for 50 $M_\odot$ stars. However, the existence of a distribution of τ_n implies that the DTD deviates from $f(\tau_{\rm gw})$ at the short delay times, because the parameter space is limited from the requirement $\tau = \tau_n + \tau_{\rm gw}$. Greggio (2005) developed a DTD for binary white dwarfs taking this effect into account. Following her results we construct the following distribution of total (nuclear + gravitational) delay time:

$$f(\tau) \propto \begin{cases} 0 & \text{if} \quad \tau < 10\,Myr \\ p_1 & \text{if} \quad 10 < \tau < 40\,Myr \\ p_2\,\tau^{0.25\beta - 0.75} \left(M_{{\rm DN},s}^{0.75(\beta + 2.33)} - M_{{\rm DN},l}^{0.75(\beta + 2.33)} \right) \\ & \text{if} \quad 40\,Myr < \tau < 13.7\,Gyr \end{cases} \tag{14}$$

where p_1 and p_2 will be chosen so as to obtain a continuous and normalized function. The first portion of the distribution ends with the formation of the first double neutron star system. Ten million years is the nuclear lifetime of a typical massive star. The second portion refers to systems which merge soon after the formation of the double neutron star binary system. Similar to the distributions in Greggio (2005), this portion of the distribution function is described as a flat plateau, up to the maximum nuclear time delay of the double neutron star binary or, in other words, the lifetime of the minimum mass progenitor of a neutron star ($\sim$9 $M_\odot$). The third portion is just the distribution of the gravitational delay times and attains to those systems for which the time delay is dominated by the gravitational radiation mechanism described by the Landau equation. The results can be seen in Fig. 2, where a normalization factor of 1 has been assumed.

2.1 Other tested DTDs

As a comparison for DTDs, we have also tested four other common options found in literature. Three of them are single-slope power laws, with $\gamma = -1.0, -1.5, -2.0$, as proposed by Côté et al. (2018b,a). We again impose a minimum value to the total delay time of 10 Myr, which represents the shortest lifetime of neutron stars progenitors. All of them are normalized between this effective minimum time and one Hubble time (13.7 Gyr). The various choices of DTDs discussed so far are shown in Fig. 2.

We also tested the DTD implemented in Matteucci et al. (2014), in which the total delay time is equal to 1 Myr on top of the stellar lifetime, implicitly assuming that all binary neutron stars are born
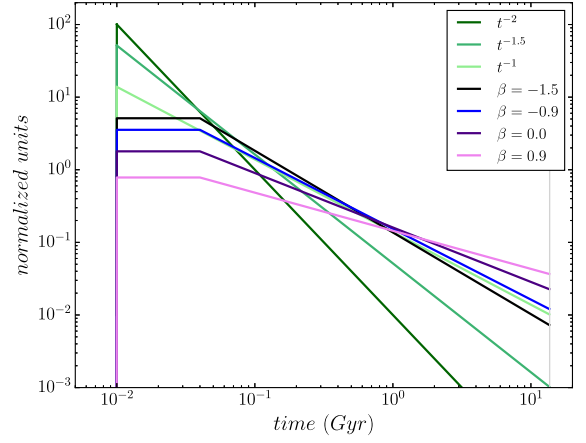
Figure 2. The seven different DTDs tested for MNS. For the DTD derived in this paper, the three phases are clearly visible: the initial null plateau, the plateau representing the close binaries that promptly merges, and the tail for wide binary systems. We have tested it for four different values of β: -1.5 (black), -0.9 (blue), 0.0 (indigo), and 0.9 (purple). The three DTDs $\propto t^{-\gamma}$ with γ equal to -1 (light green), -1.5 (medium green), and -2 (dark green) are also shown. The area under each of these curves is the same and equal to 1.

very close, and merge soon after they are formed. In Matteucci et al. (2014) it has been shown that longer gravitational delays do not reproduce the Eu abundances in very metal-poor stars.

2.2 The progenitors of SNe Ia

Since one of our constraints concerns the trend of [Eu/Fe] versus [Fe/H] and since an important part of the iron enrichment comes from SNe Ia, we need to specify a choice for their DTD. We test two different options:

(i) a distribution proportional to t^{-1}, as suggested by Totani et al. (2008) and Maoz et al. (2012) on the basis of empirical data;

(ii) the DTD in the wide double degenerate scenario depicted in Greggio (2005) with an initial separation distribution coefficient $\beta_a = -0.9$ and a maximum nuclear lifetime $\tau_{n,x} = 0.4$ Gyr. The reasons for these choices are presented in Matteucci et al. (2009).

Both DTDs are normalized in the range 0.04–13.7 Gyr, and we show them in Fig. 3. These two distributions are not very different. In fact, at times larger than $\sim$3 Gyr, the fraction of exploded SNe Ia is similar. On the other hand, as will be shown in Section 5, their effect on the [Eu/Fe] versus [Fe/H] relation at low ($-2.5 <$ [Fe/H] < -1.0 dex) metallicities is pronounced. Chemical evolution models based on DTDs very different from this kind of shape have difficulties to fit the abundances of low-metallicity stars.

The various DTDs discussed so far imply different time-scales for the Europium and Iron pollution on the ISM. As mentioned in the Introduction, the pollution time-scale can be represented as the average coalescence time-scale for a single burst stellar population, or the time within which half of the events occur. Fig. 4 shows the cumulative distribution of the DTDs for the MNS and the SNe Ia's adopted in our computations. The Europium pollution time-scales for the various models are very different, ranging from $\sim$20 Myr to 2 Gyr as the DTD for the MNS changes from the steepest pure power law to the flattest of our proposed DTD. Instead, in our models, the time-scale for Fe production from SNe Ia ranges only from 0.4 to 0.7 Gyr.
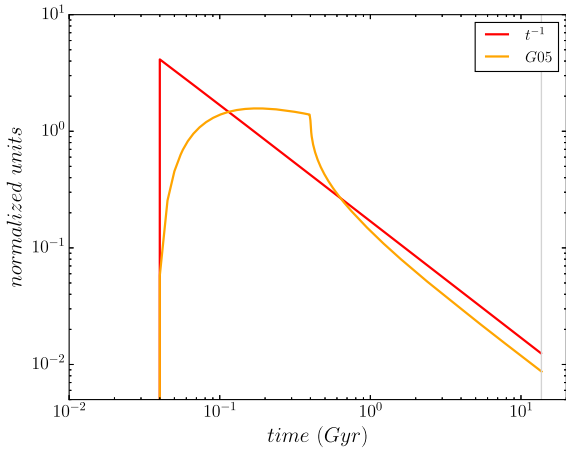
Figure 3. The two different DTDs used to represent the SNe Ia in this paper: the $\propto t^{-1}$ suggested by Totani et al. (2008) and Maoz, Mannucci & Brandt (2012; red line) and the DTD described in Greggio (2005) in the wide double degenerate case with $\beta_a = -0.9$ (orange line). This value for β_a is also suggested by Matteucci et al. (2009). The area under each of these curves is the same and equal to 1, i.e. they are normalized.
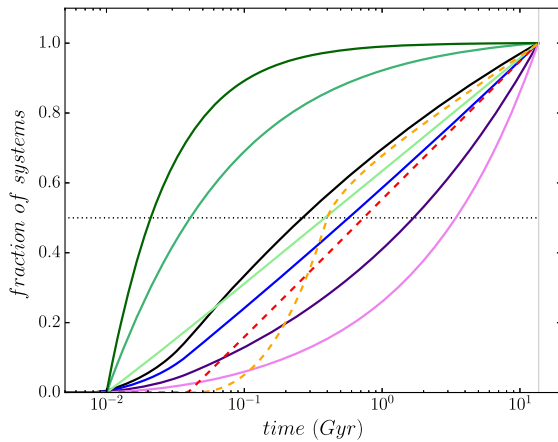
Figure 4. The cumulative distributions associated with the DTDs tested for MNS (solid lines) and for SNe Ia (dashed lines). The colour code is the same as used in Figs 2 and 3. The dotted line marks the 0.5 value for fraction of merged binary neutron stars and provide an immediate comparison between the different time-scales produced by the DTDs.

3 COMPARISON WITH THE SGRB REDSHIFT DISTRIBUTION

As briefly described in the Introduction, it has been possible to derive the SGRB redshift distribution despite the small statistics. However, there are discrepancies between the results of different groups.

3.1 The SGRB redshift distribution

To constrain our models we consider two redshift distributions of SGRB proposed in the literature: the Ghirlanda et al. (2016; hereafter G16) and Zhang & Wang (2018; hereafter ZW18).

G16 considered seven observables: (i) peak flux, (ii) fluence, (iii) observer frame duration, (iv) observer frame peak energy distribution, (v) redshift, (vi) isotropic energy, and (vii) isotropic luminosity, usually not available at the same time for each event, and

a set of parametric relations that bind these together. The parametric form chosen for the redshift is

$$\Psi(z) = \frac{1 + p_1 z}{1 + (z/z_p)^{p_2}}. \tag{15}$$

Then, they generated synthetic populations of SGRBs, choosing randomly the values of the parameters, and compared their features to the observational data set. A total of 10 free parameters (3 for redshift distribution, 3 for peak energy distribution, and 4 for energy–luminosity correlations) have been tested. This is referred in the paper as 'model a'. G16 considered also a slightly different scheme for relations between observables with independent (from the peak energy and between themselves) distributions for luminosity and duration, raising the number of free parameters to 11. This is referred as 'model c'.

The values of the redshift distribution parameters which best represent the observational characteristics of the SGRB population turn out to be: $p_1 = 2.8$ (model a) or 3.1 (model c), $p_2 = 3.5$ (model a) or 3.6 (model c), and $z_p = 2.3$ (model a) or 2.5 (model c).

With a different approach, ZW18 first considered the 16 SGRBs with known redshift. From them, they derived a peak energy–luminosity relation and have used this relation to find the redshift of the other 284 SGRBs in the *Fermi-GBM* sample. Finally, ZW18 have used these inferred redshifts to fit a bimodal relation in the form of

$$\Psi(z) \propto \begin{cases} (1+z)^{-3.08} & z < 1.60 \\ (1+z)^{-4.98} & z \geq 1.60 \end{cases}. \tag{16}$$

This is an ever-decreasing function of redshift, sharply in contrast with the result of G16.

3.2 Simulations and results

In this section we compare the SGRB redshift distribution shown above to theoretical expectations of the redshift distribution of MNS based on the DTDs described in Section 2. To do this we convolve the DTDs with the cosmic star formation rate (CSFR; see equation 1), for which we adopt the relation obtained by Madau and Dickinson (2014):

$$\Psi(z) = \frac{0.015(1+z)^{2.7}}{1 + ((1+z)/2.9)^{5.6}} \quad M_\odot \, \mathrm{Mpc}^{-3} \, \mathrm{yr}^{-1}, \tag{17}$$

based on a Salpeter (1955) IMF, that is

$$\phi(m) = 0.171 \, m^{-2.35}, \tag{18}$$

when normalized between 0.1 and 100 $M_\odot$.

For a Salpeter IMF and a 9–50 $M_\odot$ range for progenitors of NS we have $k_\alpha = 0.0059$ neutron star progenitors per $M_\odot$ of star-forming gas. The parameter α_{MNS} has been chosen in order to reproduce the current rate of GW events per unitary volume of the Universe as found by Abbott et al. (2017a), 1540 $\mathrm{yr}^{-1} \, \mathrm{Gpc}^{-3}$. The values for α_{MNS} are reported in Table 1 for the different DTDs, alongside with the fractions of MNS systems merged after 20 Myr (third column) and 100 Myr (fourth column) after an initial single star formation burst. Together with Fig. 4 this allows us to make a simple comparison among the time-scales of the different distributions.

In this way we have computed a redshift distribution of MNS rate directly comparable with the derived redshift distributions of SGRBs of G16 and ZW18. Both their relations have been multiplied by a suitable factor to reproduce the current GW rate, in order to make a comparison possible.

Table 1. The table reports the value of the occurrence probability α_{MNS} for each tested DTD that must be inserted in order to obtain the present time cosmic rate of MNS at $z = 0$ equal to the gravitational wave event rate found by the LIGO/Virgo Collaboration (Abbott et al. 2017a). In the third and fourth columns are reported the fractions of MNS systems merged after 20 and 100 Myr from a single initial starburst.

MNS DTD	α_{MNS} $(\times 10^{-2})$	Merged in 20 Myr	Merged in 100 Myr
Our DTD $\beta = 0.9$	0.66	0.008	0.056
Our DTD $\beta = 0.0$	0.81	0.019	0.129
Our DTD $\beta = -0.9$	1.02	0.039	0.241
Our DTD $\beta = -1.5$	1.18	0.056	0.336
Prop to t^{-1}	1.09	0.096	0.319
Prop to $t^{-1.5}$	1.60	0.301	0.703
Prop to t^{-2}	1.73	0.500	0.901
Constant 10 Myr	1.75	1.000	1.000

The results can be seen in Fig. 5. The rate of SGRB proposed by G16 is best represented by our DTD with $\beta = -1.5$, which means that a bottom heavy distribution (i.e. with many systems with small initial separations) is a good candidate. It is worth noting that such a value for β gives rise to a distribution of time delays, which scales as $\propto t^{-1.125}$. Lower values for β imply higher and earlier maxima, so shorter time delays are preferred. However too short time-scales, like those produced by the simple power law $\propto t^{-2}$ and the fixed 10 Myr total delay, do not produce a good agreement with the observations (see panel b of Fig. 5: the maxima appear to exceed by a large factor the G16 distributions).

The rate distribution proposed by ZW18, on the other hand, cannot be matched by any of the considered distributions. It requires a very top heavy distribution for the initial separations (with a $\beta = 6.0$) and a low probability of forming close binaries (α_{MNS} equal to 0.39×10^{-2}), but such a model is in strong contrast with the local data on chemical evolution. In fact, as it will be shown in Section 5, the chemical enrichment of our Galaxy must have happened in time-scales no longer than 30 Myr, whereas the $\beta = 6.0$ model produces time-scales far in excess of 1 Gyr.

4 CHEMICAL EVOLUTION MODEL FOR THE MILKY WAY

A chemical evolution model tracks the abundance of a given element i in the gas of a galaxy at different times. The ingredients and the general theory of such a simulation can be found, for example, in Matteucci (2012). In particular, we have adopted a scheme similar to those described in Matteucci et al. (2014) that will be summarized below.

The evolution of the surface gas density of the element i, $G_i(r, t)$, is described by the following equation:

$$\frac{dG_i}{dt}(r, t) = -\psi(r, t)Z_i(r, t)$$
$$+ \int_{m(t)}^{M_U} \psi(t - \tau(m))Q_{mi}(t - \tau(m))\phi(m) \, dm$$
$$+ Z_{i,0}A(r, t). \quad (19)$$

The first term is the product of the star formation rate (SFR) $\psi(r, t)$ and the elemental fraction $Z_i(r, t)$ in the gas and represents the gas removed by the ongoing star formation. The second term represents the fraction of gas restored as element i by stars born at $t - \tau(m)$

and dying at the time t. $\tau(m)$ is the stellar lifetime for a star of mass m. In particular, $\phi(m)$ is the initial mass function (IMF) and $Q_{mi}(t - \tau(m))$ is the production matrix for a star of mass m as defined by Talbot and Arnett (1973). M_U is the upper limit for the mass of a star that we have chosen to be 100 $M_\odot$, while $m(t)$ is the minimum mass for a star dying at the time t. The mass dying at the present time is 0.8 $M_\odot$. The third term represents the infall of gas from outside the Galaxy. This infall follows a given rate in time at each galactocentric radius $A(r, t)$ and has a primordial (i.e. given by the big bang nucleosynthesis) composition, which for element i is $Z_{i,0}$.

Our model follows the evolution of 31 chemical species, from H to Eu. The Milky Way is divided in concentric rings 2 kpc wide and equation (19) is integrated on a variable time-step, whose minimum is 2 Myr. The output quantities represent the averages (for chemical abundances) or the totals (for rates) in the simulated Galaxy. Rates are calculated for MNS and SNe Ia alike as in equation (1). We adopted the SFR by Kennicutt (1998), the IMF of Kroupa, Tout & Gilmore (1993), and a double-exponential infall law (the so-called *two infall model* of Chiappini, Matteucci & Gratton 1997) aimed at reproducing the present surface mass densities in the halo and the disc as observed by Kuijken and Gilmore (1991) with time-scales from Romano et al. (2000). No outflow is included and the instantaneous mixing approximation is retained (because their delaying effect on the chemical evolution seems negligible, see e.g. Spitoni et al. 2009). The yields are taken from Karakas (2010) for low and intermediate mass stars, from Doherty et al. (2014a,b) for super-AGB stars, from Nomoto, Kobayashi & Tominaga (2013) for SNe II, from Iwamoto et al. (1999) for SNe Ia, and from José & Hernanz (1998) for nova systems. The stellar lifetimes are those of Schaller et al. (1992).

5 COMPARISON WITH THE GALACTIC ABUNDANCES OF EUROPIUM AND IRON

In our calculation we need to specify the following parameters:

(i) the DTD of the MNS;
(ii) the DTD of the SNe Ia;
(iii) the production of Eu by CC–SNe;
(iv) the fraction of neutron stars which produce an MNS introduced in Section 2 (α_{MNS});
(v) the Eu produced per merging event.

We have varied (i) and (ii) according to the options proposed in Section 2. Concerning (iii), we have run two sets of scenarios, one in which CC–SNe are allowed to produce Eu and the other in which they are not. Finally, (iv) and (v) have been chosen according to the following observational constraints:

(i) α_{MNS} has been fixed to the value found in Section 3 to reproduce the cosmic LIGO/Virgo MNS rate (Abbott et al. 2017a);

(ii) the yield of Eu has been fixed to reproduce the solar absolute abundance of Eu observed by Lodders, Palme & Gail (2009), in particular comparing it with the simulated abundance of Eu present in the Galaxy 9 Gyr after the Big Bang (which is about the age of formation of the Solar system). Given that different values of α_{MNS} produce different predicted Eu abundances in the Sun, we have chosen a value that reproduces the observations in the case of intermediate time-scales (models 4A and 4B in Table 2) and we have kept it constant. This choice makes it easy to see the effects of different time-scales on the total amount of Eu in the solar neighbourhood.
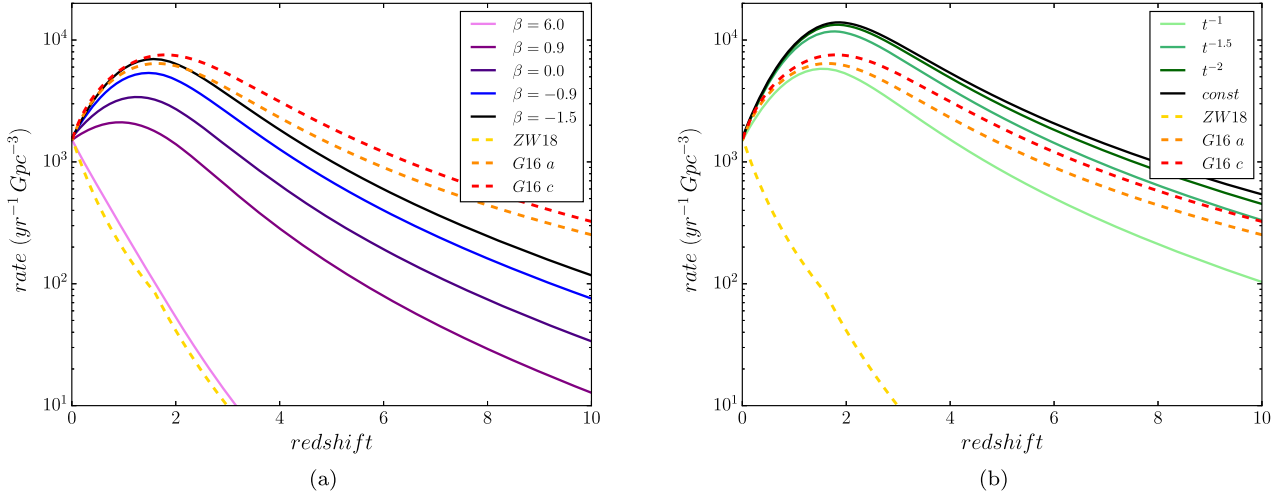
Figure 5. The redshift distribution of SGRB, as found by G16 (red and orange dashed lines) and ZW18 (yellow dashed line) against the predicted rate of MNS events (solid lines). Our DTD is shown in panel (a), with five different values for the β parameter (pink = 6.0; purple = 0.9; violet = 0.0; blue = −0.9; dark blue = −1.5). In panel (b) we show three different power laws ($\propto t^{-1}$ in light green; $\propto t^{-1.5}$ in green; $\propto t^{-2}$ in dark green) and a constant total delay of 10 Myr (in black).

Table 2. The table reports all the models shown in the graphs. As explained in Section 5, the occurrence probabilities for SNe Ia (α_{Ia}) has been tuned to obtain the current Galactic rate of SNe Ia and the current cosmic rate MNS. Instead, the occurrence probability α_{MNS} for MNS has been taken from Table 1. The yield of Eu from MNS (7th column) has been tuned to reproduce the abundance in our Sun (the results of our simulations are reported in the 9th and the 10th columns). Finally, in the 8th column is reported the predicted current rate of MNS in the Milky Way.

Name	Eu from CC–SNe	SNe Ia DTD	MNS DTD	α_{Ia} $(\times 10^{-2})$	α_{MNS} $(\times 10^{-2})$	MNS Eu yield $(\times 10^{-6} M_\odot)$	Current MNS rate (Myr^{-1})	X_{Fe} $(\times 10^{-3})$	X_{Eu} $(\times 10^{-10})$
1A	no	Prop to t^{-1}	Our DTD $\beta = 0.9$	4.77	0.66	4.0	76	1.38	1.68
2A	no	Prop to t^{-1}	Our DTD $\beta = 0.0$	4.77	0.81	4.0	84	1.38	2.29
3A	no	Prop to t^{-1}	Our DTD $\beta = -0.9$	4.77	1.02	4.0	94	1.38	3.15
4A	no	Prop to t^{-1}	Our DTD $\beta = -1.5$	4.77	1.18	4.0	102	1.38	3.77
5A	no	Prop to t^{-1}	Prop to t^{-1}	4.77	1.09	4.0	93	1.38	3.27
6A	no	Prop to t^{-1}	Prop to $t^{-1.5}$	4.77	1.60	4.0	104	1.38	4.65
7A	no	Prop to t^{-1}	Prop to t^{-2}	4.77	1.73	4.0	93	1.38	4.28
8A	no	Prop to t^{-1}	Constant 10 Myr	4.77	1.75	4.0	94	1.38	4.29
1B	no	G05 $\beta_a = -0.9$	Our DTD $\beta = 0.9$	4.67	0.66	4.0	76	1.52	1.68
2B	no	G05 $\beta_a = -0.9$	Our DTD $\beta = 0.0$	4.67	0.81	4.0	84	1.52	2.29
3B	no	G05 $\beta_a = -0.9$	Our DTD $\beta = -0.9$	4.67	1.02	4.0	94	1.52	3.15
4B	no	G05 $\beta_a = -0.9$	Our DTD $\beta = -1.5$	4.67	1.18	4.0	102	1.52	3.77
5B	no	G05 $\beta_a = -0.9$	Prop to t^{-1}	4.67	1.09	4.0	93	1.52	3.27
6B	no	G05 $\beta_a = -0.9$	Prop to $t^{-1.5}$	4.67	1.60	4.0	104	1.52	4.65
7B	no	G05 $\beta_a = -0.9$	Prop to t^{-2}	4.67	1.73	4.0	93	1.52	4.28
8B	no	G05 $\beta_a = -0.9$	Constant 10 Myr	4.67	1.75	4.0	94	1.52	4.29
1AS	yes	Prop to t^{-1}	Our DTD $\beta = 0.9$	4.77	0.66	1.5	76	1.38	2.57
2AS	yes	Prop to t^{-1}	Our DTD $\beta = 0.0$	4.77	0.81	1.5	84	1.38	2.80
3AS	yes	Prop to t^{-1}	Our DTD $\beta = -0.9$	4.77	1.02	1.5	94	1.38	3.13
4AS	yes	Prop to t^{-1}	Our DTD $\beta = -1.5$	4.77	1.18	1.5	102	1.38	3.22
5AS	yes	Prop to t^{-1}	Prop to t^{-1}	4.77	1.09	1.5	93	1.38	3.11
6AS	yes	Prop to t^{-1}	Prop to $t^{-1.5}$	4.77	1.60	1.5	104	1.38	3.68
7AS	yes	Prop to t^{-1}	Prop to t^{-2}	4.77	1.73	1.5	93	1.38	3.55
8AS	yes	Prop to t^{-1}	Constant 10 Myr	4.77	1.75	1.5	94	1.38	3.56
1BS	yes	G05 $\beta_a = -0.9$	Our DTD $\beta = 0.9$	4.67	0.66	1.5	76	1.52	2.57
2BS	yes	G05 $\beta_a = -0.9$	Our DTD $\beta = 0.0$	4.67	0.81	1.5	84	1.52	2.80
3BS	yes	G05 $\beta_a = -0.9$	Our DTD $\beta = -0.9$	4.67	1.02	1.5	94	1.52	3.13
4BS	yes	G05 $\beta_a = -0.9$	Our DTD $\beta = -1.5$	4.67	1.18	1.5	102	1.52	3.22
5BS	yes	G05 $\beta_a = -0.9$	Prop to t^{-1}	4.67	1.09	1.5	93	1.52	3.11
6BS	yes	G05 $\beta_a = -0.9$	Prop to $t^{-1.5}$	4.67	1.60	1.5	104	1.52	3.68
7BS	yes	G05 $\beta_a = -0.9$	Prop to t^{-2}	4.67	1.73	1.5	93	1.52	3.55
8BS	yes	G05 $\beta_a = -0.9$	Constant 10 Myr	4.67	1.75	1.5	94	1.52	3.56
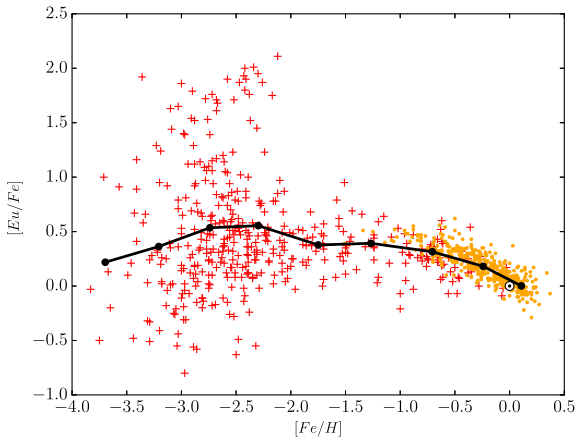
Figure 6. Observational data used in paper: a compilation of 426 Milky Way halo stars (red crosses) taken from JINABase and 374 Milky Way thin disc stars (yellow points) from Battistini and Bensby (2016). Black dots represent the average value, binned in 0.5 dex wide bins. It is possible to see the plateau at low metallicities ([Fe/H] < −1.0) and the decreasing trend at later times.

5.1 Eu production sites

As discussed in the Introduction, there are two possible sites for Eu production: MNS and CC–SNe. In this paper, we have tested two different scenarios: one in which Eu is entirely produced by MNS and another in which Eu is produced both by MNS and CC–SNe.

MNS, as a production site of Eu, have been explored thoroughly by several authors (e.g. Korobkin et al. 2012), who proposed a yield in the range $10^{-7} - 10^{-5}$ M$_\odot$ of Eu per event. More recently, the observation of the kilonova AT2017gfo has allowed us to estimate the yield of Eu in the range $(3-15) \times 10^{-6}$ M$_\odot$ of Eu per event (Evans et al. 2017; Tanvir et al. 2017; Troja et al. 2017). We have chosen to represent MNS as systems of two 1.4 M$_\odot$ neutron stars with progenitors in the 9–50 M$_\odot$ mass range.

We have chosen an empirical yield of Eu equal to 4.0×10^{-6} M$_\odot$ when the MNS are the sole producers, and 1.5×10^{-6} M$_\odot$ when Eu is co-produced by CC–SNe. This second value is slightly lower than the estimate from the kilonova AT2017gfo but well inside the theoretical range.

CC–SNe, on the other hand, have a less clear role in the r-process elements production. In this paper, we have used a slightly modified version of the provisions found in Argast et al. (2004), model SN2050, and used also in the paper Matteucci et al. (2014):

(i) a constant yield of 3.8×10^{-8} M$_\odot$ of Eu for 20–23 M$_\odot$ mass range stars;

(ii) a decreasing yield from 3.8×10^{-8} M$_\odot$ of Eu for a 23 M$_\odot$ star to 1.7×10^{-9} M$_\odot$ of Eu for a 50 M$_\odot$ star.

We do not consider any dependence on metallicity of these yields, nor do we take into account the distribution in rotational velocities of high-mass stars and its effect on the yield of Eu.

If the time-scale of Eu production were short, we would expect to see a plateau at low metallicities ([Fe/H] < −1.0) followed by a decline as the Fe abundance grows. This trend is found in the observational data (see Fig. 6), and can be explained supposing that the main producers of Fe, namely the SNe Ia, have lower mass progenitors than CC–SNe and longer gravitational delay times than MNS. Therefore, the bulk of Fe is released to the ISM on a longer time-scale with respect to Eu. Initially, Eu and Fe are

produced at a similar rate by only massive stars and this generates the plateau. Then, SNe Ia start to explode, producing Fe but not Eu, progressively decreasing the [Eu/Fe]. This behaviour is similar to that of α-elements (like O, Mg, Ca, and Si) that are likewise produced in high-mass short-lived stars, and is known as time delay model (see e.g. Matteucci 2012).

This is an idealized situation and the spread in the data for a given element can make difficult to discern between different behaviours. This is particularly true in our case of study, since the [Eu/Fe] values for halo stars span nearly three orders of magnitudes (see Fig. 6). Therefore, it is possible to identify the low-metallicity plateau only as a trend. Non-homogeneous stochastic simulations (e.g. Cescutti et al. 2015; Safarzadeh, Sarmento & Scannapieco 2018) can investigate the different spread induced by different Eu sources and it should be remarked that a model which can reproduce the mean [Eu/Fe] evolution in the halo population can still fail to account for the scatter in the data. However, here we will limit to the analysis of the average abundance trend.

5.2 Conversion of the cosmic rate to a Galactic rate

As a consistency check, we have developed a simple conversion procedure to infer the Galactic MNS rate from the cosmic LIGO/Virgo rate of Abbott et al. (2017a). We have considered the total luminosity of a unitary volume of the Universe as derived by the integration of the Press–Schechter function, equal to $2 \times 10^{17} \times h$ L$_\odot$, as reported by Mo, van den Bosch & White (2010). Here, h is the dimensionless parametrization of the Hubble constant in units of 100 km s^{-1} Mpc^{-1}.

Considering a total baryonic mass for our Galaxy equal to $(5-10) \times 10^{10}$ (as found by, for example, Sofue 2013; McMillan 2016) and a mass-to-luminosity ratio for a spiral galaxy equal to 5 (Mo et al. 2010), we have estimated the total luminosity of the Milky Way. The result is that there are $\sim(1-2) \times 10^7 \times h$ Milky Way-equivalent (MWe) galaxies per Gpc^3. Choosing a value for h equal to 0.7 as most cosmological observations suggest (Planck Collaboration XXIII 2016) produces a central value for the obtained interval of $\sim 1 \times 10^7$ MWe Gpc^{-3}. Therefore, we expect that the Galactic rate of MNS is $\simeq 10^{-7}$ times lower than the Abbott et al. (2017a) value, or $1.54^{+3.2}_{-1.22} \times 10^{-4}$ yr^{-1}. This figure compares well to previous Galactic estimations based on binary pulsars such as $0.83^{+2.1}_{-0.7} \times 10^{-4}$ yr^{-1} (Kalogera et al. 2004). In our chemical evolution model the current rate of MNS is not a free parameter, but results from the convolution of the star formation history of the Milky Way with the DTD module the fraction $\alpha_{\rm MNS}$ derived from the cosmic constraint. We will compare the model results to these figures.

5.3 Simulations and results

We ran several models, as reported in Table 2. In the 1st column we put the name of the model, in the 2nd column is indicated if the CC–SNe have been considered as production site for Eu or not, and in the 3rd and 4th columns are indicated the DTDs used, respectively, for SNe Ia and MNS. In the 5th and 6th columns are reported the values for the occurrence probabilities of SNe Ia and MNS. The occurrence probabilities $\alpha_{\rm Ia}$ have been chosen so as to obtain the estimated current rate of Type Ia supernovae, 1.8×10^{-3} *SN yr^{-1}* in the Milky Way (Li et al. 2011), while $\alpha_{\rm MNS}$ has been fixed by the local volumetric GW rate (see Section 3). In the 7th column is reported the adopted Eu yield per MNS event, in the 8th column the predicted current rate of MNS in the Milky Way and in the 9th and
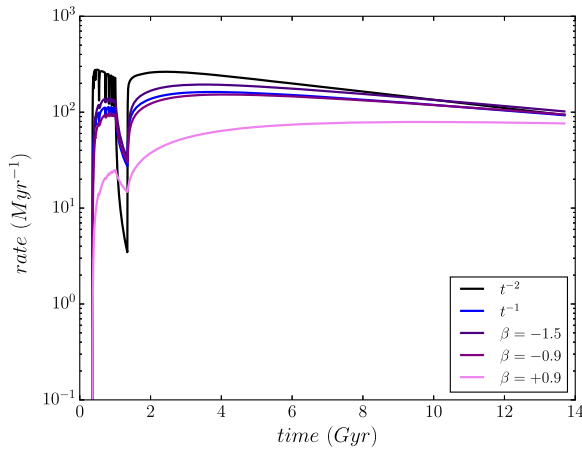
Figure 7. The Galactic rate of MNS for five of the eight DTDs tested here: 1A/B in pink, 3A/B in violet, 4A/B in indigo, 5A/B in blue, and 7A/B in black.

10th columns are reported the predicted absolute solar abundances of Fe and Eu.

As it is possible to see in Table 2, the current Galactic MNS rate turns out smaller than the estimate in Section 5.2 obtained extrapolating the Abbott et al. (2017a) value, but it appears to be in very good agreement with Kalogera et al. (2004) estimate. Given that Galactic and cosmic star formation histories are different we do expect some differences in the current MNS rate, at fixed DTD and α_{MNS}. The effect of the Galactic SFR on the MNS rate can be clearly seen in Fig. 7, where the computed MNS rates are shown: at around 1 Gyr from the formation of the Galaxy, when the first infall episode terminates, the merging rate rapidly decreases. The magnitude of such a decrease depends on the time-scale of the adopted DTD: longer ones act as smoothing masks. The rapid oscillations at very early times are caused by the threshold in the SFR adopted in the chemical model, as described in Section 4.

As a first step, it has been verified the ability of different DTDs to reproduce the solar abundances of Eu and Fe.

For the Sun, Lodders et al. (2009) have determined:

$$\log(Fe/H)_\odot = -2.792 \quad \log(Eu/Fe)_\odot = -6.496$$

$$X_{Eu} = 3.50 \times 10^{-10} \quad X_{Fe} = 1.34 \times 10^{-3}.$$

These values should be compared with the predicted ones in Table 2.

We have kept the same yields of Fe for SNe II and SNe Ia during all the tests and instead varied the DTD, using the two possible distributions listed in Section 5.1. The values reported in Table 2 show that the solar Fe abundance in our model is in excellent agreement with the observational value. For the Eu contribution from MNS, the yields were actually tuned to reproduce the solar abundance with our model. We can see that the required production is quite compatible with theoretical estimates, as well as the empirical value from of the kilonova, as mentioned in Section 5.1.

Now we can turn to study the [Eu/Fe] versus [Fe/H] relation. We remind that the [X/Y] notation refers to the logarithm of the ratio between the two elements X and Y, normalized with respect to the same logarithmic ratio in the Sun. In Fig. 8 we show the effects of different DTDs on the [Eu/Fe] versus [Fe/H] relation when CC–SNe are not allowed to produce Eu. In particular, we are interested in reproducing the decreasing trend of [Eu/Fe] versus [Fe/H] in the

disc stars (i.e. those at [Fe/H] > −1.0). We will not study the spread in the data points in the halo stars as done by other authors (e.g. Cescutti et al. 2015; Wehmeyer, Pignatari & Thielemann 2015), since our model is homogeneous. This spread is likely due to local polluting events.

We can categorize the models in three groups: those that totally fail to produce the decreasing trend in the disc stars, those that produce an insufficient decreasing trend, and those that produce an acceptable decreasing trend. The models in the first category usually fails also to reproduce the low-metallicity plateau. As it is possible to see in panels (a) and (c), the DTD derived in this paper falls in the first category, meaning that coalescence time-scales longer than 300 Myr are unable to reproduce the [Eu/Fe] versus [Fe/H] relation along the entire range of metallicities.

On the other hand, three out of four models shown in panels (b) and (d) reproduce the decreasing trend at high metallicity. The models that produce the best correspondence are the 7A/B and the 8A/B. In particular, the 7A/B also reproduce the plateau at [Fe/H] < −1.0 and can be selected as the best model. Therefore, we can say that a DTD $\propto t^{-2}$ is adequate to reproduce the [Eu/Fe] abundance pattern in the Milky Way stars, if MNS are the only contributors to Eu.

In Fig. 9 we show the models where CC–SNe co-produce Eu alongside MNS. The impact of the CC–SNe contribution is very large since with the prescriptions used here no less than 60 per cent of the solar Eu should come from CC–SNe. Here, all the DTDs produce a decreasing trend in the [Eu/Fe] versus [Fe/H] relation. In particular, DTDs with longer time-scales (like the one derived in this paper) become indistinguishable from one another (see panel a). For shorter time-scales (panel b) there are slight differences between the models. One more time, shorter DTDs (7BS, 8BS) are favoured over longer ones (5BS). The low-metallicity plateau, although deformed by the knee at [Fe/H] ∼ −3.3, is visible none the less. Such a knee is caused by the death of massive stars in the lower region (20–23 M$_\odot$) of the allowed mass range, where the yields of Eu are higher. We do not show the graphs from the 1AS to the 8AS model because they are substantially equal to those shown in Fig. 9.

In Fig. 10 we show in detail the effect of changing DTD for SNe Ia (panel a) and activating or deactivating Eu production in CC–SNe (panel b) in the abundance range [Fe/H] > −1.5. Using the G05 DTD for SNe Ia (panel a, dashed lines), that produces longer time-scales than $\propto t^{-1}$, slightly increase the steepness in [Fe/H] < −0.5, while it has substantially no impact in the [Fe/H] > −0.5. However, it is not sufficient to make our DTD (with $\beta = −1.5$) acceptable. Instead, the DTD $\propto t^{-2}$ offers an optimal profile in both cases (models 7A and 7B). If we observe panel (b), we can see that the activation of Eu production in CC–SNe strongly improves the prediction when using our DTD (model 4BS), even if it remains worse than in the case of shorter time-scales.

Finally, in Fig. 11 we show the plots relative to two popular choices for MNS: the DTD $\propto t^{-1.5}$ and the DTD $\propto t^{-1}$. We recall from Section 4 that, even if they are not the preferred models to reproduce the SGRB redshift distribution, they cannot be entirely ruled out. As we can see, we confirm what has been found by other studies (e.g. Côté et al. 2017a): a DTD $\propto t^{-1}$ is unable to recover the decreasing trend in the thin disc abundance pattern (panel a). If we activate the Eu production in CC–SNe (panel b), we obtain a relation that, although decreasing, is not sufficiently steep. A more satisfactory prediction is given by the DTD $\propto t^{-1.5}$ (models 6A/B and 6AS/BS), both with and without CC–SNe producing Eu. However, the steepness of the curve is one more time smaller than the observed one.
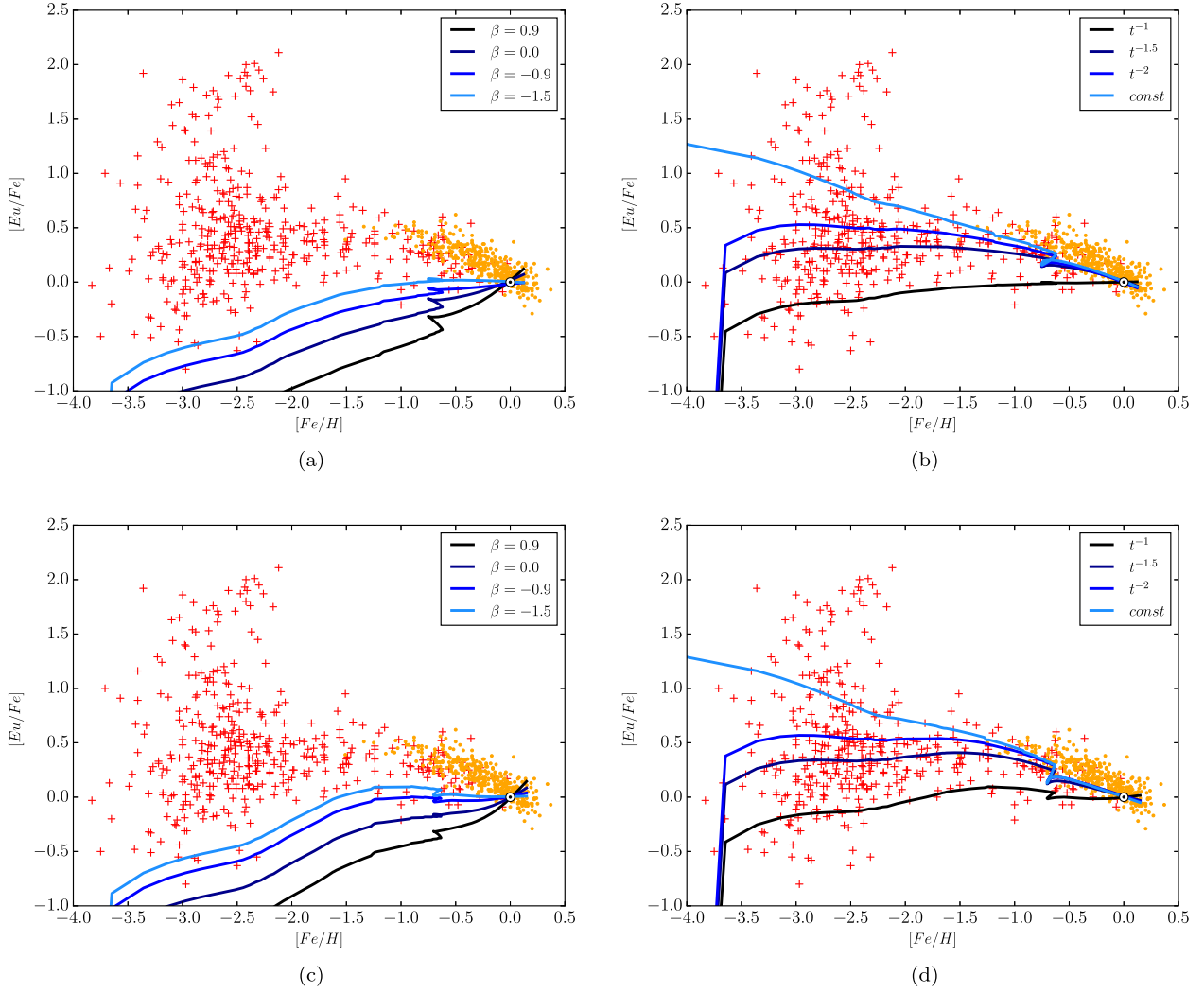
Figure 8. Here we show the models with no Eu production from CC–SNe. Panel (a) shows the models from 1A to 4A, panel (b) the models from 5A to 8A, panel (c) the models from 1B to 4B, and panel (d) the models from 5B to 8B. The colour-code is the same everywhere: lighter shades of blue stands for higher index models.
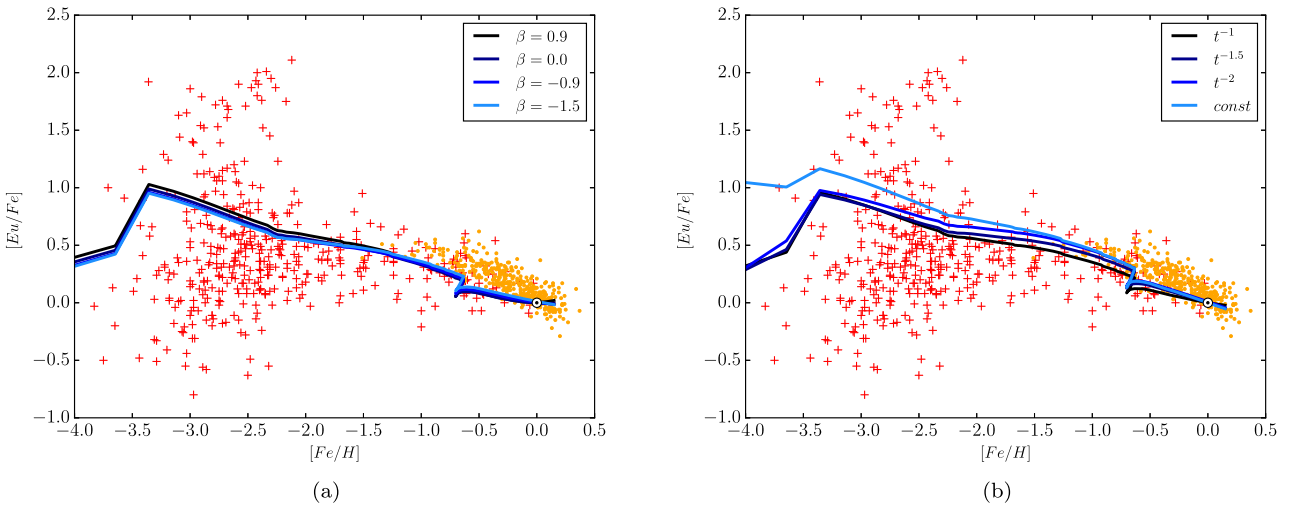
Figure 9. Here we show the models with Eu production from both CC–SNe and MNS. Panel (a) shows the models from 1BS to 4BS and panel (b) shows the models from 5BS to 8BS. The colour-code is the same everywhere: lighter shades of blue stands for higher index models.
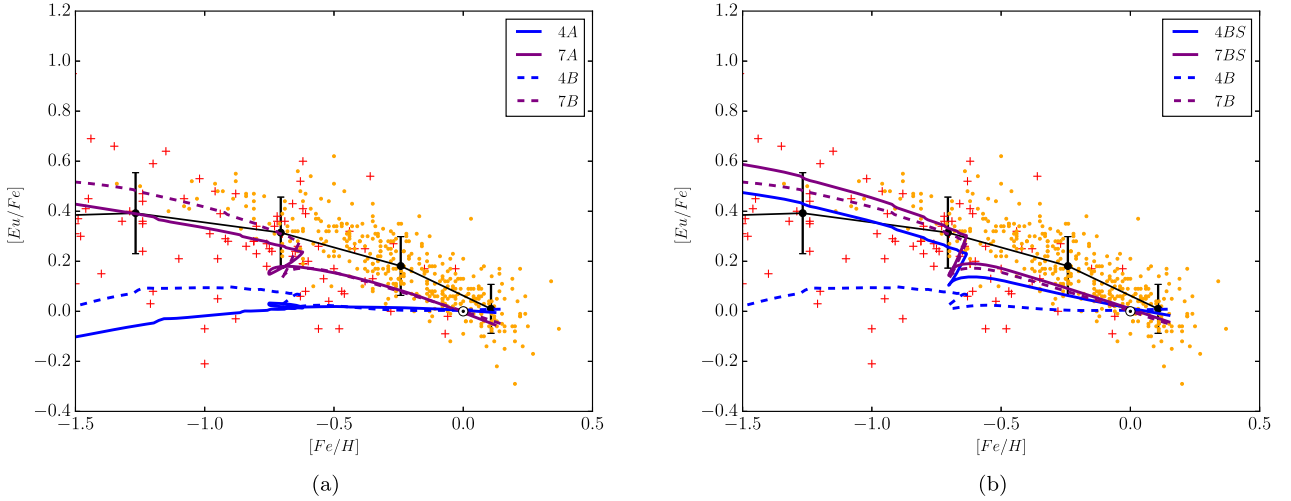
Figure 10. In panel (a) we highlight what happens when we change DTD for SNe Ia. Blue lines refer to our DTD with $\beta = -1.5$ (models 4A/B), purple lines refer to the DTD $\propto t^{-2}$ (models 7A/B). Solid lines represent models with a DTD for SNe Ia $\propto t^{-1}$ (models 4/7A), while dashed lines represent models with a G05 DTD for SNe Ia (models 4/7B). In panel (b) we highlight what happens when we activate the production of Eu in CC–SNe. Solid lines represent models where Eu is co-produced by CC–SNe (models 4/7BS), while dashed lines represent models where MNS are the sole producers of Eu (models 4/7B). Black points represents the average [Eu/Fe] in a 0.5 dex wide bin and error bars are 1σ tall.
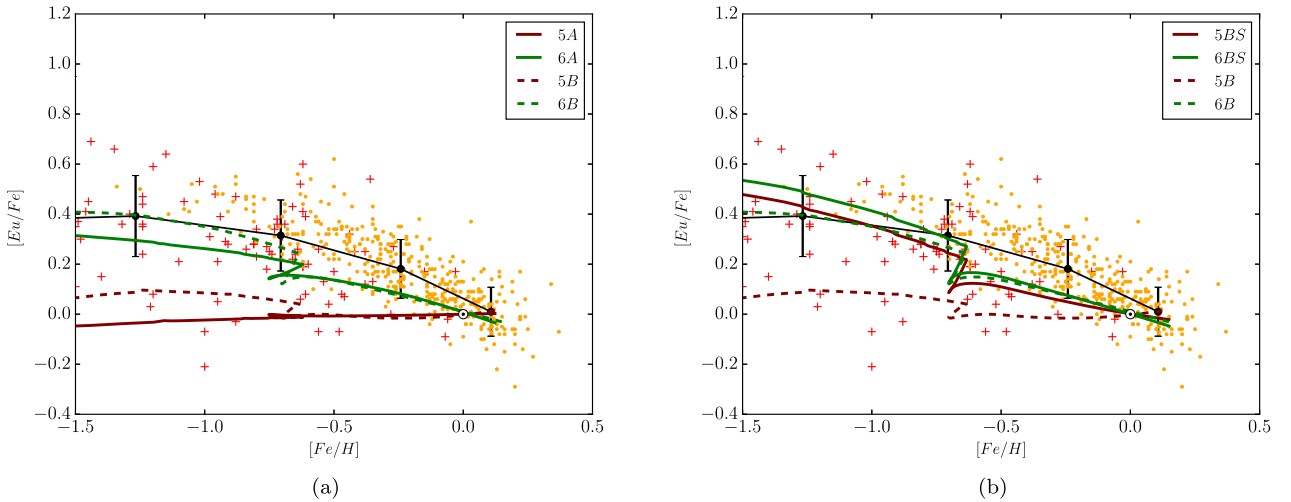
Figure 11. Brown lines refer to the DTD $\propto t^{-1}$ (models 5A/B/BS), green lines refer to the DTD $\propto t^{-1.5}$ (models 6A/B/BS). In panel (a) we highlight what happens when we change DTD for SNe Ia. Solid lines represent models with a DTD for SNe Ia $\propto t^{-1}$ (models 5/6A), while dashed lines represent models with a G05 DTD for SNe Ia (models 5/6B). In panel (b) we highlight what happens when we activate the production of Eu in CC–SNe. Solid lines represent models where Eu is co-produced by CC–SNe (models 5/6BS), while dashed lines represent models where MNS are the sole producers of Eu (models 5/6B). Black points represents the average [Eu/Fe] in a 0.5 dex wide bin and error bars are 1σ tall.

5.4 A variable α_{MNS}

CC–SNe seem to provide a way to (partially) reconcile local and cosmic data. Another possible choice is to relax the assumption of constancy of the occurrence probability of close binary neutron stars α_{MNS}. This parameter depends on the physics of the stellar formation and the efficiency of the common envelope phase in the late stages of stellar life. Population synthesis models (e.g. Giacobbo & Mapelli 2018a) indicate that metallicity plays an important role. Therefore, we tested a variation of the MNS occurrence frequency in the best-fitting model for the SGRB redshift distribution (the 4A, i.e. the one that uses the DTD derived in this paper with $\beta = -1.5$). In particular, we assumed that α_{MNS} depends on [Fe/H], called Z_{Fe} from now on. All the other parameters are left the same, as reported in Table 2, and the value for α_{MNS} reported in the table for the model

4A will be indicated as $\tilde{\alpha}_{\mathrm{MNS}}$. We tested two dependencies of α_{MNS} on Z_{Fe}:

i. model 4AV1, where α_{MNS} varies as

$$\alpha_{\mathrm{MNS}}(Z) = \begin{cases} 3\tilde{\alpha}_{\mathrm{MNS}} & Z_{Fe} \leq -1.0 \\ \tilde{\alpha}_{\mathrm{MNS}} & Z_{Fe} > -1.0 \end{cases}, \quad (20)$$

ii. model 4AV2, where α_{MNS} varies as

$$\alpha_{\mathrm{MNS}}(Z) = \begin{cases} \tilde{\alpha}_{\mathrm{MNS}}(1 + 5\ln(-Z)) & Z_{Fe} \leq -1.0 \\ \tilde{\alpha}_{\mathrm{MNS}} & Z_{Fe} > -1.0 \end{cases}. \quad (21)$$

The evolution of the parameter α_{MNS} is reported in Fig. 12. For the primordial gas, the absolute abundance of iron has been set to zero, and the initial value for α_{MNS} of 27.5 per cent has been chosen in
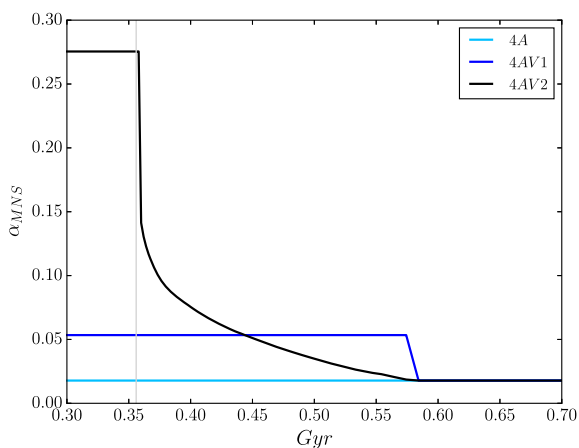
Figure 12. The evolution of the α_{MNS} parameter in three different scenarios. The grey vertical line represents the beginning of star formation in our simulation of the Milky Way.

order to best fit the observational data. Then, the sharp decrease of α_{MNS} in the model 4AV2 (black line) is produced by the rapid increase in metallicity caused by the death of the very first stars. This procedure is somewhat arbitrary but it is useful to show which variation of α_{MNS} can reconcile the SGRB cosmic rate with the [Eu/Fe] versus [Fe/H].

We have verified the ability to reproduce the current GW rate in the Milky Way and the absolute Eu abundance in the Sun. It happens that for both models 4AV1 and 4AV2, the predicted current MNS rate differs less than 0.1 per cent from the value reported in Table 2. Speaking about the absolute solar Eu abundance, the model 4AV1 predicts a value equal to 3.79×10^{-10} and the model 4AV2 predicts a value equal to 3.88×10^{-10}. Therefore, we can conclude that the impact of this enhanced early occurrence on the current MNS rate and on the total amount of Eu in the Galaxy is negligible. On the other hand, a variable α_{MNS} deeply influences the [Eu/Fe] versus [Fe/H] relation, as it is possible to see in Fig. 13. In fact, we are able to recover the decreasing trend in the disc stars, although the shape of the curve is not optimal (panel b). The model 4AV2 is also able to reproduce the low-metallicity plateau.

Finally, we have verified the impact of this new hypothesis on the cosmic rate of MNS. In order to do this, we have supposed two evolutionary patterns for the metallicity at high redshift. In the first one, the [Fe/H] evolves as predicted in the chemical evolution models of elliptical galaxies (De Masi, Matteucci & Vincenzo 2018). We have supposed a Salpeter (1955) IMF, an exponential infall on time-scales of 0.5 Gyr and an SFR efficiency of 20. These parameters produce a transition between primordial [Fe/H] values to [Fe/H] ~ -1.0 dex in 80 Myr. Instead in the second one, the [Fe/H] evolves as predicted for the Milky Way, taken as representative of the spiral galaxies, on a time-scale four times larger. The real evolution of the cosmic metallicity is expected to be intermediate between these two extreme cases. The results are shown in Fig. 14. The metallicity-dependent models differ from the non-metallicity dependent one only at very high redshift. Moreover, at least in case of a rapid chemical evolution, the predicted MNS rate does not differ too much neither at very early times. This fact demonstrates that a metallicity dependent α_{MNS} does not invalidate our derived DTD with respect to the cosmic MNS rate.

6 CONCLUSIONS

In this paper, we have derived a new DTD for MNS starting from the initial separation and mass distributions of neutron star binary systems. We have assumed a flat distribution of NS masses and a power-law distribution for the initial separations, with exponent β. We have tested four different values for β: 0.9, 0.0, −0.9, and −1.5, similar to what suggested for the DTD of SNe Ia (Matteucci et al. 2009) as derived from the double degenerate (DD) model of Greggio (2005).

We have tested our assumptions on the DTD of MNS and SNe Ia on the following constraints:

(i) the cosmic SGRB rate;
(ii) the evolution of Eu abundance in the Galaxy, in particular the [Eu/Fe] versus [Fe/H] relation.

In this context, we have also tested the effect of core-collapse SNe as producers of Eu, besides MNS. Finally, we have tested a metallicity-dependent occurrence probability for MNS (the parameter α_{MNS}). Our main results can be summarized as follows:

(i) Our derived DTD for MNS with $\beta = -1.5$ provides the best fit to the cosmic SGRB rate (as found by Ghirlanda et al. 2016). Also our DTD with $\beta = -0.9$ and the DTD going like $\propto t^{-1}$ give a good fit. With these three DTDs, the average time-scale of coalescence of MNS is 300–500 Myr. Shorter time-scales produce too many events at high redshift (2–2.5), while longer time-scales produce too few events over the entire range of redshift. This result is in agreement with the one found by Fong et al. (2017) that suggests a DTD $\propto t^{-1}$ for MNS to explain the proportion of SGRB incoming from early-type galaxies.

(ii) The other redshift distribution found by Zhang and Wang (2018) can be reproduced only with an extremely top heavy (i.e. with a lot of binaries with large separations) initial separation distribution that corresponds to use our DTD with $\beta = 6.0$. By the way, this extreme DTD cannot explain the Eu abundances in the Milky Way, independently from the contribution of CC–SNe to the Galactic Eu abundance.

(iii) When the MNS are the sole producers of Eu in the Galaxy, the models which better reproduce the [Eu/Fe] versus [Fe/H] pattern are those with short (<30 Myr) coalescence time-scales, in particular the constant total delay (stellar lifetime plus coalescence time) of 10 Myr and the $\propto t^{-2}$ distribution, in agreement with Matteucci et al. (2014) and Côté et al. (2018a). On the other hand, our derived DTD is unable to reproduce the decreasing trend of [Eu/Fe] versus [Fe/H] observed in disc stars for reasonable values of the parameter β.

(iv) When the MNS are the sole producers of Eu in the Galaxy, their yield should be no more than 4.0×10^{-6} M$_\odot$ per event. Higher yields overestimate the absolute Eu abundance in the Sun. This is in agreement with the lower end of the estimations of Evans et al. (2017) and Troja et al. (2017) in the kilonova AT2017gfo, but much higher than the estimate of Smartt et al. (2017).

(v) When CC–SNe co-produce Eu under the prescriptions of Argast et al. (2004; their model SN2050), they become the main production site and dominate the [Eu/Fe] versus [Fe/H] relation. This can reconcile the short time-scale required to explain the Eu abundance in the Milky Way with the longer time-scale required to explain the SGRB redshift distribution. However, in this case, the yield of Eu per MNS event is reduced to 1.5×10^{-6} and falls (slightly) below the range of value found by Evans et al. (2017) and Troja et al. (2017).

(a)

(b)
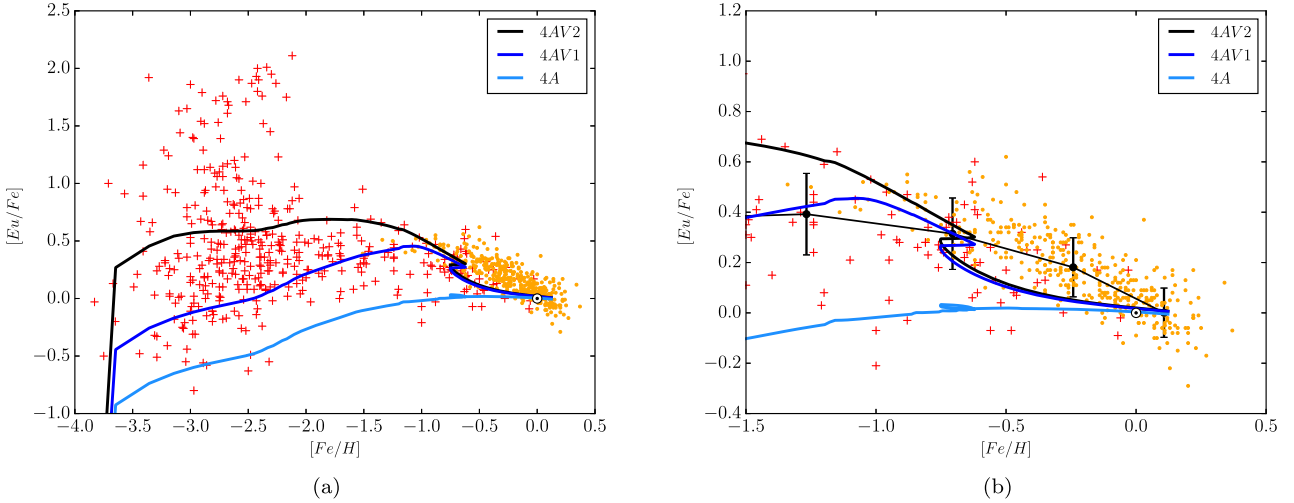
Figure 13. In these panels we show the effects of a variable MNS occurrence probability α_{MNS}. Models 4AV1 (blue line) and 4AV2 (black line) are variants of the model 4A (light blue line). In model 4AV1 we have adopted a step function for the α_{MNS}, while in model 4AV2 we have adopted a continuous function. Both of them make α_{MNS} dependent on metallicity, traced by [Fe/H]. Panel b shows in detail the behaviour of our models at [Fe/H] > -1.0.
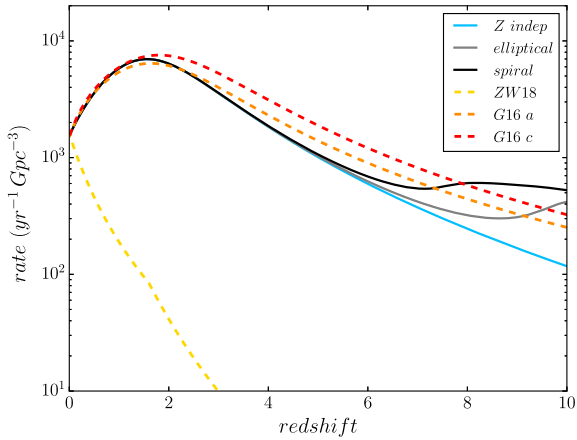
Figure 14. The predicted evolution of SGRB rate against the observed ones. The models shown are the 4A (in light blue) and the 4AV2 (black and grey lines). In particular, the grey line refers to the sub-model with a [Fe/H] evolution as predicted for an elliptical galaxy, whereas the black line refers to the sub-model with a [Fe/H] evolution as predicted for the Milky Way.

(vi) The influence of different DTDs for SNe Ia (at least of those tested here) on [Eu/Fe] versus [Fe/H] relation seems mostly negligible, and it is of the order of ~10 per cent.

(vii) The occurrence probability α_{MNS} found for SGRBs produces a Galactic rate similar to that found by Kalogera et al. (2004) from pulsar luminosities (of the order of $1-2 \times 10^{-2}$). It turns out $\alpha_{MNS} \sim 10^{-2}$, interestingly close to the occurrence probability of SNe Ia as determined form the cosmic rate of SN Ia in the local Universe (Cappellaro et al. 2015).

(viii) A metallicity-dependent occurrence probability, α_{MNS}, can increase the production of Eu at early times and at low [Fe/H] values (≤ -1.0), enabling a DTD with average coalescence time-scales of 300–500 Myr to reproduce both the SGRB redshift distribution and the [Eu/Fe] versus [Fe/H] relation in the Milky Way, when the MNS are the sole Eu producers.

In general, allowing for the CC–SNe to form Eu helps reconciling the necessity of a short time-scale in Eu production with the long time-scales required for the SGRBs. However, this choice makes single massive stars the main Eu production site, by contributing no less than ~60 per cent to the total Eu present in the Sun, and this fact is in contrast with the current understanding about heavy r-process elements nucleosynthesis. On the other hand, a time decreasing occurrence probability of MNS provides instead the correct production rate of Eu, without the contribution of CC–SNe, but this assumption is somewhat arbitrary and needs to be checked in the future by means of detailed population synthesis models.

REFERENCES

Abbott B. P. et al., 2017a, Phys. Rev. Lett., 119, 161101
Abbott B. P. et al., 2017b, ApJL, 848, 2
Antoniadis J. et al., 2013, Science, 340, 448
Arcones A., Janka H.-T., 2011, A&A, 526,, 13
Arcones A., Janka H.-T., Scheck L., 2007, A&A, 467, 1227
Argast D., Samland M., Thielemann F.-K., Qian Y.-Z., 2004, A&A, 416, 997
Battistini C., Bensby T., 2016, A&A, 586, 24
Belczynski K. et al., 2017, preprint (arXiv:1706.07053)
Berger E., 2014, ARA&A, 52, 43
Burbidge E. M., Burbidge G. R., Fowler W. A., Hoyle F., 1957, Rev. Mod. Phys., 29, 547
Cameron A. G. W., 2003, ApJ, 587, 327
Cappellaro E. et al., 2015, A&A, 584, 25

Cescutti G., Chiappini C., 2014, A&A, 565, 13

Cescutti G., Romano D., Matteucci F., Chiappini C., Hirschi R., 2015, A&A, 577, 10

Chiappini C., Matteucci F., Gratton R., 1997, ApJ, 477, 765

Côté B. et al., 2018a, preprint (arXiv:1809.03525)

Côté B. et al., 2018b, ApJ, 855, 99

Côté B., O'Shea B. W., Ritter C., Herwig F., Venn K. A., 2017a, ApJ, 835, 128

Côté B., Belczynski K., Fryer C. L., Ritter C., Paul A., Wehmeyer B., O'Shea B. W., 2017b, ApJ, 836, 230

D'Avanzo P., 2015, J. High Energy Astrophys., 7, 73

De Masi C., Matteucci F., Vincenzo F., 2018, MNRAS, 474, 5259

Doherty C. L., Gil-Pons P., Lau H. H. B., Lattanzio J. C., Siess L., 2014a, MNRAS, 437, 195

Doherty C. L., Gil-Pons P., Lau H. H. B., Lattanzio J. C., Siess L., Campbell S. W., 2014b, MNRAS, 441, 582

Eichler M. et al., 2015, ApJ, 808, 30

Eichler D., Livio M., Piran T., Schramm D. N., 1989, Nature, 340, 126

Evans P. A. et al., 2017, Science, 358, 1565

Fong W. et al., 2017, ApJL, 848, 2

Ghirlanda G. et al., 2016, A&A, 594, 13 (G16)

Giacobbo N., Mapelli M., 2018a, MNRAS, 480, 2011

Giacobbo N., Mapelli M., 2018b, MNRAS, 482, 2234

Greggio L., 2005, A&A, 441, 1055

Hotokezaka K., Kiuchi K., Kyutoku K., Okawa H., Sekiguchi Y.-i., Shibata M., Taniguchi K., 2013, Phys. Rev. D, 87, 024001

Hotokezaka K., Beniamini P., Piran T., 2018, 27, 1842005

Hulse R. A., Taylor J. H., 1975, ApJ, 195, L51

Iwamoto K., Brachwitz F., Nomoto K., Kishimoto N., Umeda H., Hix W. R., Thielemann F.-K., 1999, ApJS, 125, 439

José J., Hernanz M., 1998, ApJ, 494, 680

Kalogera V. et al., 2004, ApJ, 601, L179

Karakas A. I., 2010, MNRAS, 403, 1413

Kennicutt Jr. R. C., 1998, ApJ, 498, 541

Klebesadel R. W., Strong I. B., Olson R. A., 1973, ApJ, 182, L85

Korobkin O., Rosswog S., Arcones A., Winteler C., 2012, MNRAS, 426, 1940

Kroupa P., Tout C. A., Gilmore G., 1993, MNRAS, 262, 545

Kuijken K., Gilmore G., 1991, ApJ, 367, L9

Landau L. D., Lifshitz E. M., 1966, Klassische Feldtheorie. Akademie-Verlag, Berlin

Li W., Chornock R., Leaman J., Filippenko A. V., Poznanski D., Wang X., Ganeshalingam M., Mannucci F., 2011, MNRAS, 412, 1473

Linares M., Shahbaz T., Casares J., 2018, ApJ, 859, 1

Lodders K., Palme H., Gail H.-P., 2009, Landolt Börnstein. Springer-Verlag, Berlin, p. 712

MacFadyen A. I., Woosley S. E., 1999, ApJ, 524, 262

Madau P., Dickinson M., 2014, ARA&A, 52, 415

Maoz D., Mannucci F., Brandt T. D., 2012, MNRAS, 426, 3282

Martin D., Perego A., Arcones A., Thielemann F.-K., Korobkin O., Rosswog S., 2015, ApJ, 813, 1

Martínez-Pinedo G., Fischer T., Lohs A., Huther L., 2012, Phys. Rev. Lett., 109, 255701

Martinez J. G. et al., 2015, ApJ, 812

Matteucci F., 2012, Chemical Evolution of Galaxies. Springer-Verlag, Berlin

Matteucci F., Spitoni E., Recchi S., Valiante R., 2009, A&A, 501, 531

Matteucci F., Romano D., Arcones A., Korobkin O., Rosswog S., 2014, MNRAS, 438, 2177

McMillan P. J., 2016, Astrophysics Source Code Library, ascl:1611.006

Mo H., van den Bosch F. C., White S., 2010, Galaxy Formation and Evolution. Cambridge Univ. Press, Cambridge

Narayan R., Paczynski B., Piran T., 1992, ApJ, 395, L83

Nomoto K., Kobayashi C., Tominaga N., 2013, ARA&A, 51, 457

Norris J. P., Cline T. L., Desai U. D., Teegarden B. J., 1984, Nature, 308, 434

Özel F., Freire P., 2016, ARA&A, 54, 401

Pian E. et al., 2017, Nature, 551, 67

Planck Collaboration XXIII, 2016, A&A, 594, A23

Romano D., Matteucci F., Salucci P., Chiappini C., 2000, ApJ, 539, 235

Rosswog S., 2015, Int. J. Mod. Phys. D, 24, 1530012

Safarzadeh M., Sarmento R., Scannapieco E., 2018, preprint (arXiv:1812.02779)

Salpeter E. E., 1955, ApJ, 121, 161

Schaller G., Schaerer D., Meynet G., Maeder A., 1992, A&AS, 96, 269

Seeger P. A., Fowler W. A., Clayton D. D., 1965, ApJS, 11, 121

Siegel D. M., Barnes J., Metzger B. D., 2018, preprint (arXiv:1810.00098)

Smartt S. J. et al., 2017, Nature, 551, 75

Sofue Y., 2013, PASJ, 65, 13

Spitoni E., Matteucci F., Recchi S., Cescutti G., Pipino A., 2009, A&A, 504, 87

Talbot Jr. R. J., Arnett W. D., 1973, ApJ, 186, 51

Tanvir N. R. et al., 2017, ApJL, 848, 9

Tauris T. M. et al., 2017, ApJ, 846, 58

Totani T., Morokuma T., Oda T., Doi M., Yasuda N., 2008, PASJ, 60, 1327

Troja E. et al., 2017, Nature, 551, 71

Truran J. W., 1981, A&A, 97, 391

Vangioni E., Olive K. A., Prestegard T., Silk J., Petitjean P., Mandic V., 2015, MNRAS, 447, 2575

Wehmeyer B., Pignatari M., Thielemann F.-K., 2015, MNRAS, 452, 1970

Wheeler J. C., Cowan J. J., Hillebrandt W., 1998, ApJ, 493, L101

Winteler C., Käppeli R., Perego A., Arcones A., Vasset N., Nishimura N., Liebendörfer M., Thielemann F.-K., 2012, ApJ, 750, 5

Woosley S. E., Wilson J. R., Mathews G. J., Hoffman R. D., Meyer B. S., 1994, ApJ, 433, 229

Woosley S. E., Heger A., 2006, ApJ, 637, 914

Wu M.-R., Fernández R., Martínez-Pinedo G., Metzger B. D., 2016, MNRAS, 463, 2323

Zhang G. Q., Wang F. Y., 2018, ApJ, 852, 1 (ZW18)

This paper has been typeset from a TEX/LATEX file prepared by the author.